Elastocapillary self-folding: buckling, wrinkling, and collapse of floating filaments

Arthur A. Evans,[*a] Saverio E. Spagnolie,[*b] Denis Bartolo[cd] and Eric Lauga[e]

When a flexible filament is confined to a fluid interface, the balance between capillary attraction, bending resistance, and tension from an external source can lead to a self-buckling instability. We perform an analysis of this instability and provide analytical formulae that compare favorably with the results of detailed numerical computations. The stability and long-time dynamics of the filament are governed by a single dimensionless elastocapillary number quantifying the ratio between capillary to bending stresses. Complex, folded filament configurations such as loops, needles, and racquet shapes may be reached at longer times, and long filaments can undergo a cascade of self-folding events.

I Introduction

A common strategy for assembling intricate structures at the micro- and nano-scale is to exploit self-assembly. By introducing colloidal building blocks into soft media such as fluid interfaces, nematic liquid crystals, or more complex mesophases,[1-6] the resulting distortions of the medium can be used to fabricate more elaborate colloidal objects. Over the last ten years much effort has been devoted to achieving complex self-assembly by tailoring the shape of the elementary colloidal building blocks.[5,7] Alternatively, the existence of mechanical instabilities in elastic materials suggests a simple but elegant method for guiding the creation of complex objects: a bottom-up assembly driven by elastic instabilities in simple, flexible structures. Such a self-assembly might begin with simple building block configurations, such as straight filaments or flat sheets, which when coupled to another medium would fold or wrinkle to minimize the total energy of the system.[8-11] If the system is well characterized theoretically, the dominant force balance can be tuned to yield desirable shapes. Recent examples include the use of adhesion and delamination,[12-18] and swelling and capillary interactions.[19-21]

When particles are confined to a fluid interface, their interactions are mediated through the surface deformations.[2,22] The deformations and thus the surface energy of the fluid may be decreased by a rearrangement of the particles on the surface, leading to effective capillary forces which can be attractive or repulsive depending on the geometry, density differences, and wetting properties of the particles. For two identical particles, the forces are always attractive. This so-called "Cheerios effect," and similar surface-mediated aggregation have been investigated in the context of vesiculation,[23,24] colloidal flocculation,[2,6] and millimetric ecology.[25,26] While there have been many studies on filaments and polymers that interact *via* short-range forces and/or external flow fields,[27-38] the impact of long-range capillary forces on the shapes of flexible filaments lying on a fluid interface remains unexplored.

In this paper we consider the problem of elastocapillary self-folding of a flexible micro-filament. The model system, illustrated in Fig. 1, is that of a flexible filament confined to a fluid interface. The balance between long-range capillary forces, which are attractive between different parts of the filament, and bending stresses resisting deformation can lead to a novel buckling instability (as illustrated in Fig. 1b), and at longer times to highly deformed folded patterns in the filament. Herein we show how to harness the shape instability to fabricate folded structures. The paper is organized as follows. In Section II we introduce the setup and discuss the energetics of the system. In Section III we pose the non-dimensional problem to solve for the shape dynamics in a viscous fluid. The linear stability analysis for the shape is presented in Section IV, where we determine the functional dependence of the most unstable wavelength on both filament and fluid properties, as well as the effect of external tensile forces. We show that the threshold for self-buckling depends on a single dimensionless parameter quantifying the ratio between self-attraction and bending akin to the recently introduced elastocapillary number.[19] The complex, folded filament configurations reached far from the threshold of instability are explored by numerical simulations in Section V. We close with a discussion of our main findings in Section VI.

aDepartment of Chemistry and Biochemistry, University of California Los Angeles, 405 Hilgard Ave, Los Angeles, CA 90095, USA. E-mail: artevans@ucla.edu

bDepartment of Mathematics, University of Wisconsin-Madison, 480 Lincoln Drive, Madison, WI 53706, USA. E-mail: spagnolie@math.wisc.edu

cPMMH, CNRS, ESPCI ParisTech, Universités Paris 6 & Paris 7, 10 rue Vauquelin, 75231 Paris cedex 05, France

dLaboratoire de Physique de lEcole Normale Supérieure de Lyon, Universitté de Lyon and CNRS, 46, allée d'Italie, F-69007 Lyon, France

eDepartment of Mechanical and Aerospace Engineering, University of California San Diego, 9500 Gilman Drive, La Jolla, CA 92093, USA
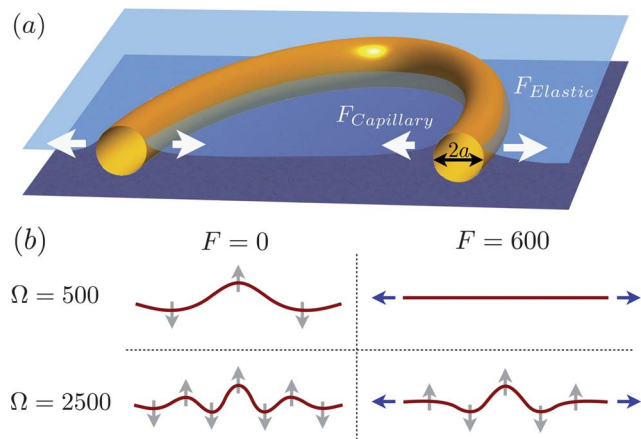
Fig. 1 The model system considered in the paper. (a) A flexible filament (of radius a) floating at the interface between two fluids. Every part of the filament experiences capillary attraction to every other part while bending resists deformation. The competition between capillary forces and bending results in buckling and folding. (b) The most unstable wavelength depends on a dimensionless strength of self-attraction, Ω. The onset of this instability can be tuned with the introduction of an added tension from an external source, F, which also decreases the most unstable wavelength (the shapes shown are obtained using the numerical computations).

II   Energy and Scaling

Consider two identical particles of size a located at the interface between two fluids, for example air and water. Provided the distance between the particles, R, is much smaller than the capillary length, their effective capillary interactions are described by the interaction energy $E_{int} = \gamma a^2 \ln(R/\ell_c)$, where γ is the interaction strength per unit area and the capillary length is defined by $\ell_c = \sqrt{\sigma/\rho g}$, with σ the surface tension of the interface, ρ the difference in density between the two fluids, and g the acceleration due to gravity ($\ell_c \approx 2$ mm for an air–water interface).[39] The strength of the interaction comes from the competition between surface forces and an external force monopole.[2] This force can originate from gravity, as in the case of the "Cheerios effect",[22] or from electro- or magneto-static forces;[4] note that γ contains additional information such as the particle geometry and wetting properties.

For microscopic systems, the energetic contribution from capillary monopoles are individually very weak.[40,41] As a result, most studies of these systems neglect monopoles from buoyancy, and in the absence of external torques, the leading order singular contribution comes from quadrupolar interactions.[42,43] In the case of anisotropic particles, this quadrupolar interaction, while relatively short ranged, can lead to remarkably complex colloidal aggregation and directed assembly.[44,45] However, there is some subtlety associated with the monopole term, and it lies in the very long-ranged nature of the interaction it produces. Although pairwise contributions are very weak, the screening length for the interaction is much larger than the system size itself, and thus the total energetic contribution from monopoles can significantly effect the behavior of the system.[2]

The model system considered in this paper is illustrated in Fig. 1. We consider an inextensible elastic filament of length $L < \ell_c$ and bending modulus B. The filament bending energy is

$$E_{bend} = \frac{B}{2} \int_0^L |x_{ss}|^2 ds + \frac{1}{2} \int_0^L T(s) \left[|x_s|^2 - 1 \right] ds, \quad (1)$$

where $x(s,t)$ denotes the two-dimensional position vector of the filament on the fluid surface at time t. The arc-length coordinate parameterizing the filament is denoted by s, subscripts denote partial derivatives, and $T(s)$ is a Lagrange multiplier enforcing the inextensibility condition. For notational simplicity in the following we will commonly assume an implicit dependence upon time.

The contribution to the energy due to capillary monopole interactions may be written as

$$E_{int} = \int_0^L \int' \gamma \ln \left[\frac{R(s,s')}{\ell_c} \right] ds' ds, \quad (2)$$

where $R(s,s') = |x(s) - x(s')|$, γ is now the energy per area of the interaction between two points on the filament, and where we have defined $\int' = \int_{-a}^{s-a} + \int_{s+a}^{L+a}$, with a the size of the short-length cutoff (a is typically of the order of the filament radius). This cut-off radius represents the region where our long-ranged assumption of monopole interactions breaks down. In writing eqn (2) we have assumed the pairwise additivity of the long-range capillary interactions. This assumption is similar to the approach used to derive the leading-order term in a slender-body theory for Stokes flows where the hydrodynamics of a continuous rod is approximated by that of a discrete super-position of beads; this yields excellent predictions due to the long-range nature of the underlying hydrodynamic interactions.[46]

Scaling distances by the filament length, L, the tension $T(s)$ by B/L^2, and energies by B/L, the total energy combining bending and interaction takes the simple form:

$$E = \int_0^1 \left\{ \frac{1}{2} |x_{ss}|^2 + \frac{1}{2} T(s) \left[|x_s|^2 - 1 \right] + \Omega \int' \ln R(s,s') ds' ds \right\}. \quad (3)$$

E depends on a single dimensionless parameter, $\Omega = \gamma L^3/B$, which quantifies the balance between capillary self-attraction and bending, and is akin to the so-called elastocapillary number.[19]

Next, we focus on deriving the equation of motion for a filament relaxing to equilibrium, which we will then exploit to analyze shape instabilities.

III   Equations of motion

To perform detailed calculations of the filament dynamics, we consider variations of the total energy, E, with respect to the centerline position vector, $x(s)$, and tension, $T(s)$. The forces so derived must balance with the forces generated by the motion through the fluid, which we model through a local drag coefficient, ζx_t, an appropriate approach for dynamics in a very viscous fluid. The ambient fluid is assumed to be quiescent and of infinite extent. Scaling time upon the characteristic time scale $\tau = L\zeta/B$, we arrive at a dimensionless equation for the motion of the filament,

$$\boldsymbol{x}_t = -\boldsymbol{x}_{ssss} + \Omega \int' \frac{\boldsymbol{x}(s') - \boldsymbol{x}(s)}{R(s',s)^2} \mathrm{d}s' + \partial_s(T(s)\boldsymbol{x}_s). \qquad (4)$$

Anticipating our numerical approach, the local part of the integration in eqn (4) may be handled analytically by adding and subtracting the singular part of the integrand. In so doing, we find

$$\int' \frac{\boldsymbol{x}(s') - \boldsymbol{x}(s)}{R(s',s)^2} \mathrm{d}s' = \boldsymbol{K}[\boldsymbol{x}(s')](s) + c(s)\boldsymbol{x}_s(s) + O(\delta \log \delta), \qquad (5)$$

$$\boldsymbol{K}[\boldsymbol{x}(s')](s) = \int_{-\delta}^{1+\delta} \left\{ \frac{\boldsymbol{x}(s') - \boldsymbol{x}(s)}{R(s',s)^2} - \frac{\boldsymbol{x}_s(s)}{s'-s} \right\} \mathrm{d}s', \qquad (6)$$

where $c(s) \equiv \log[(1 + \delta - s)/(s + \delta)]$, with $\delta = a/L$ the dimensionless short wavelength cut-off. Rewriting the dimensionless filament position equation, we therefore have

$$\boldsymbol{x}_t = -\boldsymbol{x}_{ssss} + \Omega c(s)\boldsymbol{x}_s(s) + \Omega \boldsymbol{K}[\boldsymbol{x}(s')](s) + \partial_s(T(s)\boldsymbol{x}_s). \qquad (7)$$

Classically, the equation for the tension $T(s)$ is derived using the relation $\boldsymbol{x}_s \cdot \boldsymbol{x}_{ts} = 0$, and also the identities

$$\boldsymbol{x}_s \cdot \boldsymbol{x}_{ss} = 0, \ \boldsymbol{x}_s \cdot \boldsymbol{x}_{sss} = -\boldsymbol{x}_{ss} \cdot \boldsymbol{x}_{ss}, \qquad (8)$$

$$\boldsymbol{x}_s \cdot \boldsymbol{x}_{ssss} = -3\boldsymbol{x}_{ss} \cdot \boldsymbol{x}_{sss}, \ \boldsymbol{x}_s \cdot \boldsymbol{x}_{sssss} = -4\boldsymbol{x}_{ss} \cdot \boldsymbol{x}_{ssss} - 3\boldsymbol{x}_{sss} \cdot \boldsymbol{x}_{sss}, \qquad (9)$$

yielding the differential equation

$$\left(\partial_{ss} - |\boldsymbol{x}_{ss}|^2\right)T(s) = -\left[4\boldsymbol{x}_{ss} \cdot \boldsymbol{x}_{ssss} + 3|\boldsymbol{x}_{sss}|^2\right] - \Omega c_s(s)$$
$$- \Omega \boldsymbol{x}_s \cdot \frac{\partial}{\partial s}\boldsymbol{K}[\boldsymbol{x}(s')](s). \qquad (10)$$

Boundary conditions are derived by including terms to the energy functional to account for the work done in forcing the endpoints to move, namely, $E_F = -\boldsymbol{F}_0 \cdot \boldsymbol{x}(0) - \boldsymbol{F}_1 \cdot \boldsymbol{x}(1)$, where $\boldsymbol{F}_0$ and $\boldsymbol{F}_1$ are (dimensionless) externally applied forces at the $s = 0$ and $s = 1$ endpoints of the filament, respectively. Assuming that the filament ends are free, hinged about a specified (possibly moving) point, or pulled by the forces defined above, the solvability conditions thus require

$$\boldsymbol{x}_{ss}(0) = \boldsymbol{x}_{ss}(1) = 0, \qquad (11)$$

$$-\boldsymbol{F}_0 + \boldsymbol{x}_{sss}(0) - T(0)\boldsymbol{x}_s(0) = 0, \qquad (12)$$

$$-\boldsymbol{F}_1 - \boldsymbol{x}_{sss}(1) + T(1)\boldsymbol{x}_s(1) = 0. \qquad (13)$$

The boundary conditions are then found to be

$$\boldsymbol{x}_{sss}(0) = (\boldsymbol{I} - \boldsymbol{x}_s(0)\boldsymbol{x}_s(0)^T)\boldsymbol{F}_0, \qquad (14)$$

$$\boldsymbol{x}_{sss}(1) = -(\boldsymbol{I} - \boldsymbol{x}_s(1)\boldsymbol{x}_s(1)^T)\boldsymbol{F}_1, \qquad (15)$$

$$T(0) = -\boldsymbol{F}_0 \cdot \boldsymbol{x}_s(0), \ T(1) = \boldsymbol{F}_1 \cdot \boldsymbol{x}_s(1). \qquad (16)$$

To summarize, the partial differential equation describing the motion of a floating filament with either free or forced ends is given by eqn (7) with the boundary conditions shown in eqn

(11), (14) and (15). It is coupled to the equation for the tension, eqn (10), with boundary conditions shown in eqn (16). The numerical method developed to solve this system of equations is described in Appendix A. In the next section we exploit our equations of motion to describe the linear stability of the filament.

IV Linear stability analysis

A Numerical investigation of growth rates

Before we pursue an analytical description of filament instability, let us begin with a brief numerical investigation using the framework described in Appendix A. In order to consider the growth rate σ (in time) of a given wavenumber k, we seed a nearly straight filament with the perturbed dimensionless shape $\boldsymbol{x}(s) = (x(s), y(s)) = (s, a_0 \sin(ks))$, with $a_0 = 10^{-4}$, and we make the assumption that $y(s,t) \approx a_0 \sin(ks)e^{\sigma t}$ for small time t. Ten timesteps are then taken with a step-size $\Delta t = 10^{-9}$, and the growth rate is computed as $\sigma = \log(a_{10}/a_0)/(10\Delta t)$, where $a_{10} = 2\int_0^1 \sin(ks)y(s, 10\Delta t)\mathrm{d}s$. Fig. 2a shows (as symbols) the growth rates computed for two different interaction strengths when the filament ends are left free. For $\Omega = 140$, we find that there are no wavenumbers for which the growth rate is positive, indicating that the filament is linearly stable to transverse perturbations. Despite the attraction of every part of the filament to every other part, the filament's stiffness prevents the buckling and subsequent collapse when the body is perturbed from a straight conformation. Conversely, increasing the interaction strength to $\Omega = 2000$, the capillary attraction overcomes the bending elasticity and we observe that the filament is linearly unstable. A wide range of wavenumbers corresponds to positive growth rates. It is worth noting that the critical value of the interaction strength above which capillary interactions destabilize the filament is much larger than 1, suggesting that it could not have been inferred solely from dimensional analysis. We also show in Fig. 2b the growth rates computed for two different interaction strengths, where an external pulling force has been introduced at the filament ends. For a given interaction strength the external force reduces the growth rate of every mode, and so decreases the value of the largest unstable mode. Meanwhile, setting $F > 0$ introduces a negative slope in σ for small k, and significantly increases the value of the smallest unstable mode; the range of wavenumbers k corresponding to the unstable modes is reduced when an external tension is applied.

B Analytical predictions

Having gained intuition from the numerical simulations described above, we now turn to an analytical investigation of filament instability. Our goal is to establish the dispersion relation governing the bending excitations of a floating elastic filament.

One exact solution to the complete floating filament system is the possibly unstable trivial solution, that of a straight filament lying along a director, taken here to be $\hat{\boldsymbol{x}}$ without loss of generality. While an imbalance of external forces can be handled without difficulty, let us consider the case where the
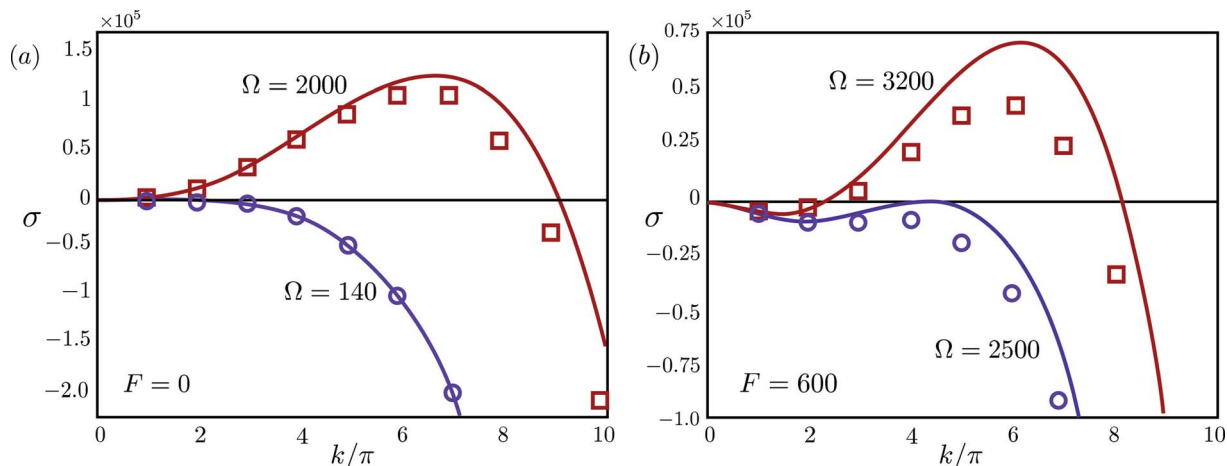
Fig. 2 Instability of the filament shape: exponential growth rate, σ, computed numerically (symbols) and predicted analytically (eqn (24), lines). (a) With no external force, $F = 0$, we consider two interaction strengths $\Omega = 140$ (just below the critical value $\Omega_c = 144$ for the instability), and $\Omega = 2000$. (b) With an external force $F = 600$, we consider the values $\Omega = 2500$ and $\Omega = 3200$.

endpoint forces are equal in magnitude and acting parallel to the long axis of the filament, $\boldsymbol{F}_0 = -F\hat{\boldsymbol{x}}$, $\boldsymbol{F}_1 = F\hat{\boldsymbol{x}}$. The trivial filament position is then given by $\boldsymbol{x}^*(s) = s\hat{\boldsymbol{x}}$. Eqn (10) indicates that the tension in this state satisfies $\partial_{ss}T^*(s) = -\Omega c_s(s)$, with $T(0) = T(1) = F$, and hence

$$T^*(s) = F + \Omega \left(s\int_0^1 c(s')\mathrm{d}s' - \int_0^s c(s')\mathrm{d}s' \right). \quad (17)$$

The tension along the straight filament is given by the force applied at the filament endpoints, as well as a renormalized contribution owing to the capillary self-attraction. This internal compression is a consequence of the non-local deformation of the fluid surface.

From here, we are well-situated to perform a classical stability analysis based on perturbations of both $\boldsymbol{x}(s)$ and $T(s)$. To begin, we write $\boldsymbol{x}(s,t) = s\hat{\boldsymbol{x}} + \varepsilon\tilde{y}(s,t)\hat{\boldsymbol{y}} + O(\varepsilon^2)$, and let $T = T^* + \tilde{T}$, with T^* the equilibrium tension from eqn (17). By tracking terms of size ε and smaller, it may be shown that at leading order, the non-local contribution to the capillary force only gives rise to a transverse force contribution as

$$\boldsymbol{K}[\boldsymbol{x}(s')](s) = O(\varepsilon^2)\hat{\boldsymbol{x}} + \varepsilon\int_0^1 \left[\frac{\tilde{y}(s') - \tilde{y}(s)}{(s' - s)^2} - \frac{\tilde{y}_s}{s' - s} \right]\mathrm{d}s'\hat{\boldsymbol{y}}. \quad (18)$$

Upon the insertion of $\dfrac{\partial}{\partial s}\boldsymbol{K}[\boldsymbol{x}(s')](s) = O(\varepsilon^2)\hat{\boldsymbol{x}} + O(\varepsilon)\hat{\boldsymbol{y}}$ into eqn (10), we deduce that $T = T^* + O(\varepsilon^2)$, such that we may dispose of tension perturbations $\tilde{T}$ for the linear stability analysis. Similarly, we find that $\hat{\boldsymbol{x}} \cdot \boldsymbol{x}_t = O(\varepsilon^2)$ from eqn (7), so that the linear stability consideration may focus solely on transverse filament motions through the evolution of $\tilde{y}(s,t)$.

In order to gain physical insight for the nonlocal operator $\boldsymbol{K}$ given by eqn (18), we assume that s is sufficiently far removed from the filament endpoints and look at its effect on plane waves of wavenumber k. By doing so, we find that the transverse component of $\boldsymbol{K}[\boldsymbol{x}(s')](s)$ may be written as

$$\boldsymbol{K}[\boldsymbol{x}(s')](s)\hat{\boldsymbol{y}} \approx g(k)\tilde{y}(s), \quad (19)$$

where

$$g(k) = 2[1 - \cos(k) + \gamma + \log(k) - kS_i(k) - C_i(k)], \quad (20)$$

and with the sine and cosine integrals defined by

$$S_i(k) = \int_0^k \frac{\sin(t)}{t}\mathrm{d}t, \quad C_i(k) = -\int_k^\infty \frac{\cos(t)}{t}\mathrm{d}t. \quad (21)$$

The mathematical details of this derivation are provided in Appendix B. Combining the results above, the transverse component of the filament position equation, eqn (7), gives a linear relation for $\tilde{y}(s)$,

$$\tilde{y}_t = -\tilde{y}_{ssss} + \Omega g(k)\tilde{y} + [\Omega c(s) + T_s^*]\tilde{y}_s + T^*\tilde{y}_{ss} + O(\varepsilon^2). \quad (22)$$

Upon inspection of T^*, we are reminded that the local self-attraction term $c(s)$ could just as well have been absorbed into the tension, and simplifying the above results in

$$\tilde{y}_t = -\tilde{y}_{ssss} + T^*\tilde{y}_{ss} + \Omega g(k)\tilde{y}. \quad (23)$$

We are thus left with the relatively simple over-damped Euler–Bernoulli beam equation, with a non-uniform tension, and with an additional term of magnitude Ω originating from the non-local capillary attraction. In the following we discuss in detail the impact of this novel effective elasticity term on the dynamic response of the floating filament.

In order to explore the response of the filament shape to small perturbations, we explicitly insert the ansatz $\tilde{y} = e^{iks+\sigma t}$. While the finite-size effects must come into play for small wavenumbers and for longer times (trigonometric functions do not satisfy the boundary conditions on eqn (23), for example), this ansatz is expected to be accurate far from the end points of the filament. Upon insertion of the equilibrium tension $T^*(s)$, an inner product of eqn (23) against e^{-iks} reveals the dispersion relation for the growth rate,
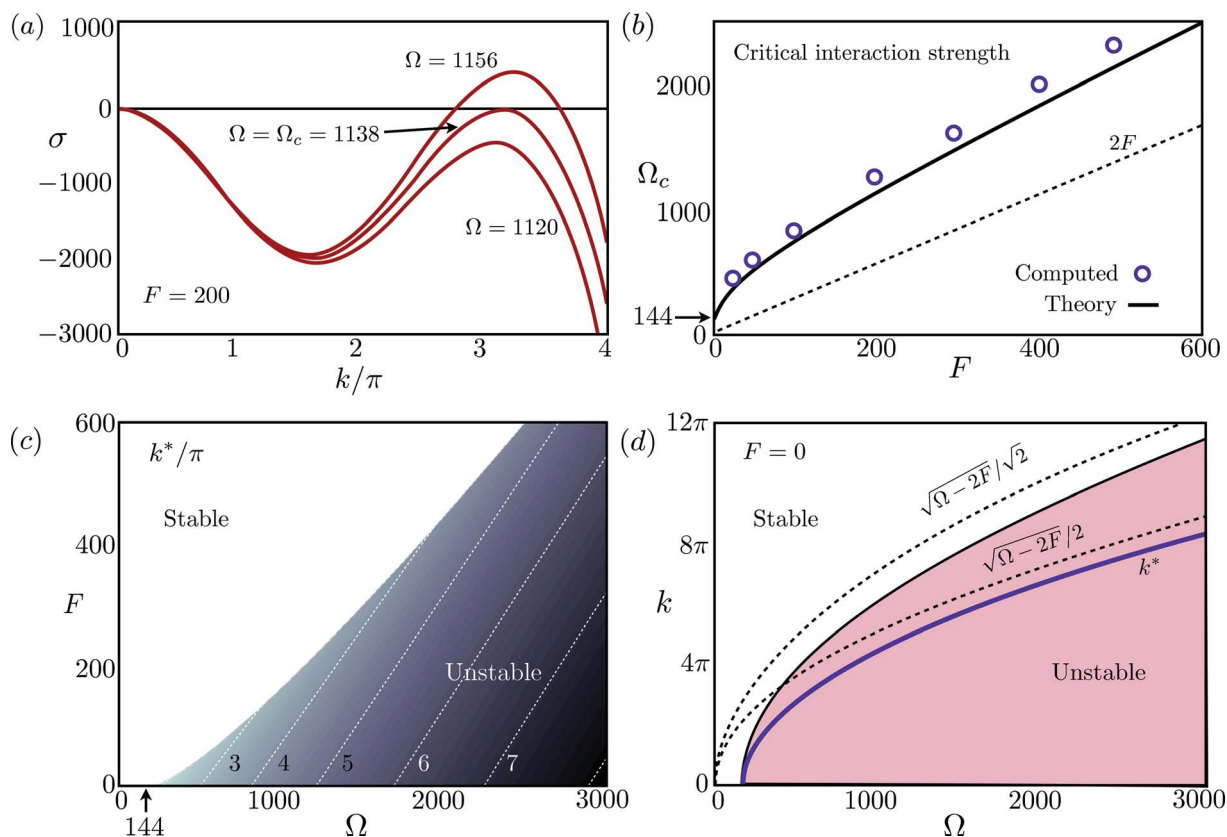
Fig. 3 (a) Growth rate of the instability, σ, as a function of wavenumber, k, for three values of the interaction strength, Ω, with external force $F = 200$ (the value of the critical interaction strength is $\Omega_c = 1138$). (b) Critical interaction strength, Ω_c, below which there are no unstable modes as a function of the external force, F, from both numerical simulations (symbols) and analytical prediction (line). (c) Map of the most unstable mode, k^*/π, analytically predicted (from eqn (24)) as a function of Ω and F. (d) Setting $F = 0$ (free filament ends), the most unstable wavenumber, k^*, is surrounded by an increasingly wide band of unstable modes as Ω increases (shaded region); analytical estimates for the most unstable and the highest unstable mode are shown as dashed lines.

$$\sigma = -k^4 + \frac{1}{2}k^2(\Omega - 2F) + \Omega g(k). \qquad (24)$$

How well does the analytical expression above capture the results of the full numerical simulation? Returning to Fig. 2a and b, the analytically predicted growth rates from eqn (24) are shown as lines for each of the four cases considered. While discrepancies are expected due to end effects, which are not captured in our asymptotic consideration, in general we find good agreement between the numerical and analytical results. Therefore, we can use eqn (24) with confidence to demonstrate the fundamental physics behind the elastocapillary instability, which we do below.

C Discussion of the elastocapillary instability

The quartic term and quadratic terms in eqn (24) are associated with the canonical Euler buckling. However, as expected, the capillary attraction leads to an additional compressive load (the Ωk^2 term in eqn (24)). Any attractive short-range coupling along the filament is expected to renormalize the tension term in a similar fashion. We now discuss the consequence of the more complex contribution, $\Omega g(k)$, to the dispersion relation. We first stress that $g(0) = 0$, and $g(k) < 0$ for all $k > 0$, which means that

the non-local part of the capillary coupling acts to stabilize straight conformations.

In addition, given that $\Omega \geq 0$ and $F \geq 0$, the predicted growth rate σ goes to zero as $k \to 0$, to $-\infty$ as $k \to \infty$, and may or may not take on positive values for finite k, depending on the values of Ω and F. For example, Fig. 3a shows the growth rate from eqn (24) as a function of wavenumber k for three values of the interaction strength, Ω, with an external pulling force $F = 200$. For Ω less than a critical value, $\Omega_c = 1138$ in this case, all modes are predicted to decay in time, and the filament is predicted to be stable. For $\Omega > \Omega_c$, we observe the appearance of a band of unstable modes and the filament becomes unstable. The critical interaction strength for instability, Ω_c, is shown as a function of the value of F in Fig. 3b. It takes the value $\Omega_c = 144$ when $F = 0$ and increases with increasing F. Both the values predicted by the analytical theory and those found by the full numerical simulation are shown; here again we see that the analysis is sufficient to capture the linear instability of the filament dynamics.

To develop physical insight into this behavior, we look at at the asymptotic form of $\sigma(k)$ in the limit of long wavelengths. We find that $\sigma \sim -Fk^2 + (\Omega/144 - 1)k^4$ for $k \ll 1$. In this regime, the capillary-induced compressive load vanishes; the self-attraction

does not renormalize the tension of the filament in the long wavelength limit. Nevertheless, the capillary coupling softens the filament by effectively reducing its bending stiffness: the pre-factor of the quartic term decreases linearly with Ω, and changes its sign at $\Omega_c = 144$. Above this critical value the bending excitations along the filament are amplified. As noted in the previous section, this unexpectedly high value of Ω_c could not have been anticipated on the basis of dimensional arguments alone. Furthermore, as $\partial\sigma/\partial k < 0$ as $k \to 0$ for any $F > 0$ the smallest unstable mode, if there is one, must take on a finite value when an external pulling force is applied.

Beyond this prediction of the destabilization threshold, we can also accurately predict the value of the most unstable mode, which chiefly sets the ultimate folded shape of the filament as we will show more precisely in the next section. For a given force F and interaction strength Ω (such that $\Omega > \Omega_c$), the most unstable mode $k^\star$ is recovered upon setting $\partial\sigma/\partial k$ to zero and solving for k. The resulting value is presented in Fig. 3c as a function of both Ω and F. Predictably, the most unstable mode increases with increasing self-attraction (increasing Ω), and decreases as the filament ends are pulled upon with greater intensity (increasing F). The introduction of an external force renders the filament stable for small interaction strengths Ω, and so intuitively prolongs the onset of buckling. Increasing Ω and/or decreasing F is therefore expected to yield a more finely folded filament shape once the instability fully develops.

In the specific case of a free filament, $F = 0$, Fig. 3d shows the value of most unstable wavenumber as a function of Ω. The shaded region indicates the band of unstable modes for a given interaction strength Ω. Again, these variations can be qualitatively understood by inspecting the asymptotic behavior of $\sigma(k)$. Indeed, for $k \gg 1$ we find $\sigma(k) \sim -k^4 + \Omega[k^2 - \pi k + 2(\log(k) + \gamma + 1)]$, with γ the Euler–Mascheroni constant. This latter approximation of $\sigma(k)$ is accurate to within 2% of the exact value for wavenumbers as small as $k = \pi$, and it can therefore replace $\sigma(k)$ generally for all but the very longest perturbation wavelengths. For $k \gg 1$, the problem boils down to the canonical Euler buckling induced by the longitudinal self-attraction. Hence, balancing the cubic and linear terms in the equation $\partial\sigma/\partial k = 0$ gives the usual approximation to the most unstable mode:[47]

$$k^* \approx \frac{1}{2}\sqrt{\Omega - 2F}. \qquad (25)$$

The largest unstable mode may also be predicted, again assuming $k \gg 1$, by setting $\sigma \approx -k^4 + (\Omega/2 - F)k^2 = 0$, yielding $k_{max} \approx \sqrt{\Omega - 2F}/\sqrt{2} = \sqrt{2}k^\star$. These approximations are shown as dashed lines in Fig. 3d. Both overestimate their true values in the present study but capture the numerical results qualitatively. The reason for this discrepancy is due to the range of relevant wavenumbers involved in the elastocapillary instability. Destabilization of the bending modes occurs at small or intermediate values of the wavenumber k; the non-local corrections to the Euler-buckling problem ($\Omega g(k)$ terms in eqn (24)) thus cannot be overlooked and strongly contribute to the dynamic response of floating microfilaments.

In summary, we have shown in this section through a linear stability analysis that a self-attracting filament displays a novel

mechanical instability. We have explored the structure of this instability, and its dependence on both the strength of the self-attraction and the stabilizing external force.

V   Beyond linear-stability: self-folding of a floating filament

The linear stability analysis of the previous section yields some insight into how folding will begin. In this section we investigate long-term, large-amplitude folding behavior. The path that a filament takes towards any final configuration depends on the initial conditions, the material parameters of the system (specified completely by Ω), and the external tension on the filament (F). In this section we compute the dynamics from the equations of motion described in Section III using the numerical method described in Appendix A.

For large values of the interaction parameter the capillary attraction overcomes the relatively weak bending resistance, and the filament displays a tendency to "accordion": it collapses with a short wavelength relative to the filament length. The dynamics of such filament self-folding are shown in Fig. 4a, where we plot the value of the total energy E (eqn (3)) as a function of time, fixing $\Omega = 2500$ and $F = 0$ for two different initial filament shapes. The topmost curve (blue online) shows the path taken of a filament that is seeded with an initial transverse position $y(s,0) = 0.05 \sin(\pi s)$ as it travels down to a state of lower energy. At short times the shape is predominately composed of a number of anti-nodes corresponding to the fastest growing wavenumber, predicted by maximizing eqn (24) to be $k^\star = 7.4\pi$. These anti-nodes grow to form loops, and eventually the filament approaches a regime of near-contact. In this vicinity there is a slight discontinuity in the slope of the energy, as a result of introducing near-field repulsive physics required to regularize the diverging capillary interactions (see Appendix A). The lower curve in Fig. 4a (red online) shows the path taken by an identical filament seeded with a different initial condition, $y(s,0) = 0.05\sin(7\pi s)$. Here the filament eventually achieves the same conformation as in the previously considered case, dictated by the fastest growing linear mode. However, due to its initial shape being closer to the fastest growing linearly unstable mode at the outset, this filament begins its descent into lower energy conformations earlier. Interestingly, this result suggests that the elastocapillary buckling provides a robust means to achieve complex foldings of microfilaments. Indeed, the gross features of the ultimate shapes can be anticipated from a simple linear stability analysis.

By introducing an external tension, $F > 0$, the possibilities for folding become more versatile but more complex. In Fig. 4b we show three different filaments, all with initial positions given by $y(s,0) = 0.05\sin(\pi s + 0.01s)$ (a shape with a slight left-right asymmetry), but pulled upon with three different magnitudes of external forcing ($F = 0$, 500, and 800). With the addition of this external tension the most unstable mode structure is changed, and a different final state is selected. With no external tension ($F = 0$), the filament accordions tightly as in Fig. 4a. In the second case, with $F = 500$, the fastest growing unstable wavenumber is shifted to a smaller value, as predicted by the linear
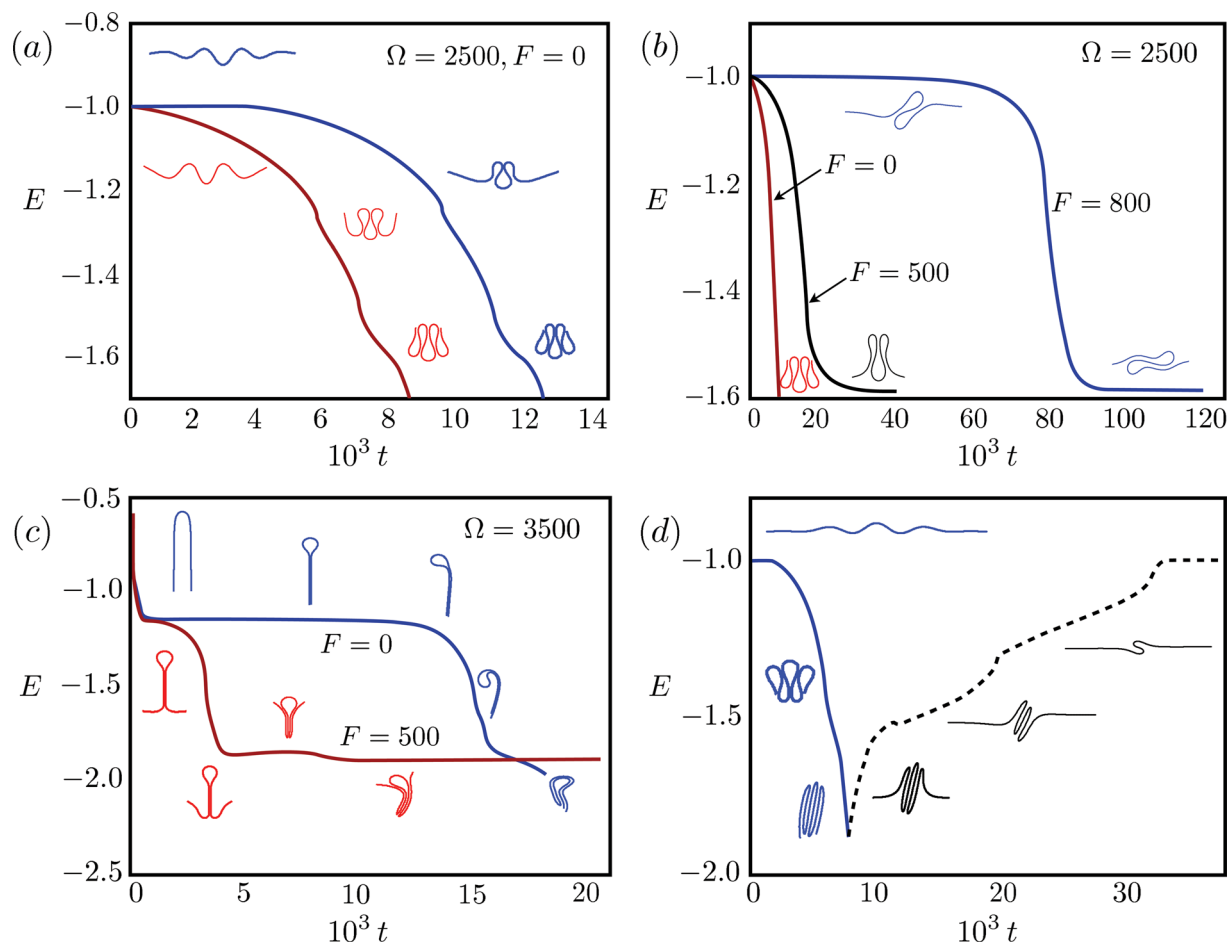
Fig. 4 Long-time dynamics of filament shape. (a) With $\Omega = 2500$ and $F = 0$, two initial perturbations with different initial wavenumbers ($k = \pi$, top and $k = 7\pi$, bottom) fold into similar structures but at different times. (b) Adding an external force, F, modifies the folding shape of the filament; with $\Omega = 2500$ and $F = 500$, the final folded shape has fewer loops than in the $F = 0$ case due to the straightening influence of the added tension. Meanwhile, for $F = 800$ a secondary instability develops along the axial direction, leading to a final left-right asymmetric shape. (c) With $\Omega = 3500$, a highly deformed initial hairpin configuration undergoes a cascade of self-folding events. (d) Folding and unfolding of a floating filament is shown for $\Omega = 3500$; the filament self-folds with $F = 0$ until $t = 9 \times 10^{-3}$ at which time a pulling force $F = 3500$ is introduced and the filament unzips, albeit through a different path through shape space.

theory, leading to a smaller number of loops in an equilibrium conformation. Finally, with $F = 800$ we observe a secondary instability growing along the axial direction, perpendicular to the transverse instability at the center of the previous section.

In fact, when a filament is sufficiently long relative to the structures generated by the initial instability, it can undergo a cascade of instabilities. This is illustrated in Fig. 4c, where we seed the filament initially with the shape of a hairpin. In the absence of external forcing, the hairpin shape is seen to first "zip up" into a racquet shape, reminiscent of the ones observed in wetted fibers,[19] and in semi-flexible polymer systems.[27,28] Over time it displays a cascade of buckling and folding. By pulling on the filament ends with an external force, $F = 500$, similar multiply folded states are obtained, yet the final shape is markedly different from the one observed in the force-free case.

Finally, in Fig. 4d we illustrate the unfolding of a self-folded structure. The filament is set initially with the shape $y(s,0) = 0.05\sin(7\pi s)$, and we fix $\Omega = 3500$ and $F = 0$. The shape

evolves in a similar fashion as in the previously described examples (blue solid line). At $t = 9 \times 10^{-3}$, we introduce external forcing on the filament ends with magnitude $F = 3500$ to unfold (black dashed line). We observe an unzipping of the folded structure, with jumps in the filament energy indicative of each loop being pulled apart in succession. Rather than a reversible shape change we clearly observe unfolding along a different path.

VI Conclusion

In this paper we have described the elastocapillary instability of flexible filaments confined to a fluid surface. Buckling and folding result from the interplay between self-attraction through long-range capillary forces and elastic bending rigidity. As a result of the competition between these mechanical forces, the instability only appears beyond a large, critical ratio of the capillary self-attraction to the filament's bending modulus. The most unstable wavenumbers are typically located at an

intermediate range, thereby yielding the spontaneous formation of accordions folds. Due to the long-range nature of the capillary interactions, both the wavelength and the growth rate of this instability differ from the conventional Euler-buckling results, which would be observed for short-range self-attraction.

After having analyzed the onset of filament shape instability through a linear theory, numerical simulation was used to show a number of possible conformational transitions for the self-folding filament. In particular, introducing an external pulling force at the filament ends changes the unstable linear modes, and modifies significantly the long-time behavior. For a filament sufficiently long relative to the shapes driven by self-attraction there can be a cascade of folding instabilities, each acting perpendicularly to the previous fold. While the linear analysis is only valid for short times and nearly straight filaments, our simulations demonstrate a wide variety of accessible conformations, from rackets and sewing needles to accordion shapes.

The numerical method described here could be augmented to study many related problems. Future work might include computing the relative energy scales for each equilibrium shape; with sufficient statistics, the ensemble of different shapes that could be expected should our system be coupled to a thermal bath might be elucidated. The deterministic simulations could also be used to determine the statistical significance of certain shapes in crumpled thin sheets or fibers.[48,49]

Our original experimental motivation was provided by buoyant particle interactions, where the dominant competition is between elasticity and the density of the particles. In which practical experimental setup could the buckling instability be observed? We recall that the critical elastocapillary number is given by $\Omega = \gamma L^3/B$. The instability is expected to be observable for filaments both soft (small value of B) and dense (large value of γ). Consider a filament composed of microns-sized spherical colloids linked by double-stranded DNAs as in ref. 50. From capillary interactions we expect $\gamma \sim F^2/\sigma$ where F is the force per unit length acting on the filament and σ the surface tension of the fluid interface. From gravity we get $F \sim \Delta\rho a^2 g$ and thus $\gamma \sim \Delta\rho^2 a^4 g^2/\sigma$. For colloids of radius $a = 10\ \mu m$ and $\Delta\rho = 10^3$ kg m^{-3} and an interface with $\sigma \sim 10^{-2}$ N m^{-1} we would get $\gamma \sim 10^{-10}$ N m^{-1}. Using filaments of length $L \sim 1$ mm, right below the capillary length, and with a DNA linker flexibility of $B \sim 10^{-22}$ J m^{-1},[50] we would obtain an elastocapillary number or order $\Omega \sim 10^3$, and thus the instability could be observable. Obviously, beyond the case of gravitational forcing, any external force acting on the filament can serve to deform the interface and drive similar elastocapillary self-folding. Electric or magnetic fields acting on self-assembled filaments of metallic nanoparticles or super-paramagnetic nano filaments could be two experimental examples.

Appendix A: numerical solution

The numerical approach taken in this manuscript is a variation on that described by Tornberg and Shelley.[51] The complications present here are the stiffness introduced by the elastic restorative term $\propto x_{ssss}$, and the nonlocal integral operator $K[x(s')]$.

The approach will be to treat the stiffest terms implicitly in time, while treating the remaining terms explicitly for a fast but stable scheme.

Time is discretized uniformly, with the nth timestep denoted by t_n, and writing (for instance) the tension at the nth timestep in shorthand as $T(s, t_n) = T^n(s)$. At each time t_n the tension is first solved *via*

$$(\partial_{ss} - |x_{ss}^n|^2)T^n(s) = -\left[4x_{ss}^n \cdot x_{ssss}^n + 3|x_{sss}^n|^2\right] - \Omega c_s(s)$$
$$- \Omega x_s^n \cdot \frac{\partial}{\partial s} K[x^n(s')](s) + \beta(1 - x_s \cdot x_s). \quad (A1)$$

We have included a correction term to remove numerical errors in the determination of the arc-length, again following Tornberg and Shelley. To solve this equation we define a uniform grid $s = i/M$, for $i = 0,1,...,M$. Spatial derivatives computed using second-order accurate finite difference formulae. Since the position x^n at time t_n is known, the equation above is inverted to recover $T_n(s)$ without difficulty.

Solving the filament position equation is the next step, where we update *via*

$$\frac{1}{2\Delta t}\left(3x^{n+1} - 4x^n + x^{n-1}\right) = -x_{ssss}^{n+1} + \Omega c(s)(2x_s^n - x_s^{n-1})$$
$$+ \Omega K\left[2x^n(s') - x^{n-1}(s')\right](s)$$
$$+ \partial_s\left(2T^n x_s^n - T^{n-1}x_s^{n-1}\right).$$

For the first time step the above is replaced by a first order Euler step. In this case, we need only build the following matrix operator and to invert it once: $M = 3/(2\Delta t)I + D_s^4$ (along with boundary conditions). The inverted operator may be applied to known quantities at every subsequent time step, providing for a very efficient numerical scheme. We have subtracted off the singular part inside the integrand of the interaction forcing so that the remainder of the expression is finite, as described in the main text.

A challenging numerical problem is introduced when the filament comes into near contact with itself. Or worse, when the filament exhibits a large number of loops so that there are many near-contact interactions. The situation is illustrated in Fig. 5, where two different parts of the filament are shown nearing each other; the centerline is denoted by dotted lines, and the blue solid lines indicate the thickness of the filament.
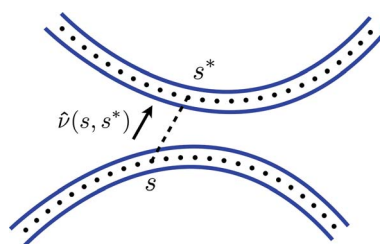

Fig. 5 A near-contact situation; s^* denotes the point on the filament closest to the station s.

Our intention is to prevent filament crossing, but to allow for tangential motions in the near-contact state. For each station in arc-length on the filament s, we first determine the closest point on the filament s^* that is at least a distance 4ε from s (so as to neglect neighboring points on the filament),

$$s^*(s) = \min_{s'}\{|\boldsymbol{x}(s') - \boldsymbol{x}(s)|, \, |s' - s| > 4\varepsilon\}. \tag{A2}$$

A local coordinate system is then defined by $\hat{\nu}(s,s^*) = (\boldsymbol{x}(s^*) - \boldsymbol{x}(s))/|\boldsymbol{x}(s^*) - \boldsymbol{x}(s)|$ and $\hat{\eta} = \hat{\nu}^\perp$. The forces in the filament equation are then decomposed locally into their $\hat{\nu}$ and $\hat{\eta}$ components. The tangential component of the filament force balance is left unchanged, but the normal component is adjusted as follows

$$\hat{\nu}(s,s^*)\cdot(\boldsymbol{x}_t + \boldsymbol{x}_{ssss}) = \min\Big\{\hat{\nu}(s,s^*)\cdot\boldsymbol{G}, \hat{\nu}(s,s^*)\cdot$$
$$\boldsymbol{G}\Big[1 - \Big(\frac{2\varepsilon}{|\boldsymbol{x}(s) - \boldsymbol{x}(s^*)|}\Big)^p\Big]\Big\} \tag{A3}$$

where $\boldsymbol{G}$ denotes the right hand side of eqn (7) (minus the stiffest term, $\boldsymbol{x}_{ssss}$), and $p > 0$ (we use $p = 12$ for all the results presented here). The multiplication factor is such that there is no normal component of force (outside of the elastic part) when the filament centerline is 2ε away from the closest point on the other part of the filament centerline. The minimum of the two quantities is chosen so that if the fluid and tension forces wish to separate the filaments from each other they can, but if the fluid and tension forces are pushing the filaments to an overlapped state the sign of this force is reversed. This treatment of the near-contact physics appears to allow the filament to fold up tightly without numerical difficulties, without significantly impacting the underlying physics of capillary attraction. When the filament comes into near-contact, the timestep size is decreased and the spatial resolution is increased adaptively.

For the linear stability analysis we set $M = 2000$, $\Delta t = 10^{-9}$, $\beta = 5 \times 10^6$. For the long-time dynamics and equilibrium shapes it was sufficient to set $M = 600$, $\Delta t = 10^{-8}$, $\beta = 5 \times 10^6$, and $p = 12$, with adaptive refinement of the grid and decrease in timestep size as necessary when the filament approached itself as described.

Appendix B: nonlocal integration

We begin by showing, for $k \gg 1$ and s sufficiently far removed from the filament endpoints, that

$$K[\tilde{y}(s)] = \int_0^1 \Big\{\frac{\tilde{y}(s') - \tilde{y}(s)}{(s' - s)^2} - \frac{\tilde{y}_s(s)}{s' - s}\Big\}\mathrm{d}s' \approx -\pi k\tilde{y}(s), \tag{B1}$$

for $\tilde{y}(s) \propto \sin(ks)$. For $k \gg 1$, we are led to write the integration over a new inner variable $s' = s + \xi/k$, so that

$$K[\tilde{y}(s)] = k \int_{-ks}^{k(1-s)} \Big\{\frac{\sin(ks') - \sin(ks)}{\xi^2} - \frac{\cos(ks)}{\xi}\Big\}\mathrm{d}\xi, \tag{B2}$$

and for s well distanced from both endpoints, we may approximate the above as

$$K[\tilde{y}(s)] \approx k \int_{-\infty}^{\infty} \Big\{\frac{\sin(ks + \xi) - \sin(ks)}{\xi^2} - \frac{\cos(ks)}{\xi}\Big\}\mathrm{d}\xi$$
$$= k\sin(ks) \int_{-\infty}^{\infty} \frac{(\cos(\xi) - 1)}{\xi^2}\mathrm{d}\xi + k\cos(ks) \int_{-\infty}^{\infty} \frac{\sin(\xi) - \xi}{\xi^2}\mathrm{d}\xi \tag{B3}$$
$$= -\pi k\sin(ks) = -\pi k\tilde{y}(s).$$

Though we do not reproduce it here, a complicated analytical expression for $K[\tilde{y}(s)]$ in eqn (B1) may in fact be derived for arbitrary wavenumber k. While it is not generally the case that $K[\tilde{y}(s)]$ is diagonalized using a trigonometric basis (as it is in the $k \gg 1$ approximation above), we still note that

$$\int_0^1 e^{-iks} K[e^{iks'}]\mathrm{d}s = g(k), \tag{B4}$$

$$g(k) = 2[1 - \cos(k) + \gamma + \log(k) - k\,S_i(k) - C_i(k)], \tag{B5}$$

with the sin and cosine integrals defined in eqn (21). For $k \ll 1$ we have $g(k) \sim -k^2/2$, while for $k \gg 1$ we have $g(k) \sim -\pi k + 2(\log(k) + \gamma + 1)$, with γ the Euler–Mascheroni constant. This latter approximation of $g(k)$ is accurate to within 2% for wavenumbers as small as $k = \pi$.

Acknowledgements

References

1 G. M. Whitesides and B. Grzybowski, *Science*, 2002, **295**, 2418.

2 A. Dominguez, M. Oettel and S. Dietrich, *Phys. Rev. E: Stat., Nonlinear, Soft Matter Phys.*, 2010, **82**, 011402.

3 L. Ramos, T. C. Lubensky, N. Dan, P. Nelson and D. A. Weitz, *Science*, 1999, **286**, 2325.

4 P. A. Kralchevsky and K. Nagayama, *Adv. Colloid Interface Sci.*, 2000, **85**, 145.

5 C. P. Lapointe, T. G. Mason and I. I. Smalyukh, *Science*, 2009, **326**, 1083.

6 W. Russel, D. A. Saville and W. R. Schowalter, *Colloidal Dispersions*, Cambridge University Press, 1989.

7 S. Sacanna, W. T. M. Irvine, P. M. Chaikin and D. J. Pine, *Nature*, 2010, **464**, 575.

8 Y. Klein, E. Efrati and E. Sharon, *Science*, 2007, **315**, 1116.

9 J. Huang, M. Juszkiewicz, W. de Jeu, E. Cerda, T. Emrick, N. Menon and T. Russell, *Science*, 2007, **317**, 650.

10 X. Chen and J. Yin, *Soft Matter*, 2010, **6**, 5667.

11 B. Li, Y. Cao, X. Feng and H. Gao, *Soft Matter*, 2012, 5728–5745.

12 D. P. Holmes and A. J. Crosby, *Phys. Rev. Lett.*, 2010, **105**, 038303.

13 B. Audoly, *Phys. Rev. E: Stat., Nonlinear, Soft Matter Phys.*, 2011, **84**, 011605.

14 D. Vella, M. Adda-Bedia and E. Cerda, *Soft Matter*, 2010, **6**, 5778.

15 H. Diamant and T. A. Witten, *Phys. Rev. Lett.*, 2011, **107**, 164302.

16 L. Pocivavsek, R. Dellsy, A. Kern, S. Johnson, B. Lin, K. Y. C. Lee and E. Cerda, *Science*, 2008, **320**, 912.

17 F. Brau, H. Vandeparre, A. Sabbah, C. Poulard, A. Boudaoud and P. Damman, *Nat. Phys.*, 2011, **7**, 56.

18 A. A. Evans and E. Lauga, *Phys. Rev. E: Stat., Nonlinear, Soft Matter Phys.*, 2009, **79**, 066116.

19 B. Roman and J. Bico, *J. Phys.: Condens. Matter*, 2010, **22**, 493101.

20 S. H. Kang, N. Wu, A. Grinthal and J. Aizenberg, *Phys. Rev. Lett.*, 2011, **107**, 177802.

21 S. H. Kang, B. Pokroy, L. Mahadevan and J. Aizenberg, *ACS Nano*, 2010, **4**, 6323.

22 D. Vella and L. Mahadevan, *Am. J. Phys.*, 2005, **73**, 817.

23 I. Koltover, J. O. Rädler and C. R. Safinya, *Phys. Rev. Lett.*, 1999, **82**, 1991.

24 B. J. Reynwar, G. Illya, V. A. Harmandaris, M. M. Muller, K. Kremer and M. Deserno, *Nature*, 2007, **447**, 461.

25 D. L. Hu and J. W. M. Bush, *Nature*, 2005, **437**, 733.

26 J. Voise, M. Schindler, J. Casas and E. Raphal, *J. R. Soc. Interface*, 2011, **8**, 1357.

27 B. Schnurr, F. C. MacKintosh and D. R. M. Williams, *Europhys. Lett.*, 2000, **51**, 279.

28 B. Schnurr, F. Gittes and F. C. MacKintosh, *Phys. Rev. E: Stat., Nonlinear, Soft Matter Phys.*, 2002, **65**, 061904.

29 U. Seifert, W. Wintz and P. Nelson, *Phys. Rev. Lett.*, 1996, **77**, 5389.

30 O. Hallatschek, E. Frey and K. Kroy, *Phys. Rev. Lett.*, 2005, **94**, 077804.

31 O. Hallatschek, E. Frey and K. Kroy, *Phys. Rev. E: Stat., Nonlinear, Soft Matter Phys.*, 2007, **75**, 031905.

32 Y.-N. Young, *Phys. Rev. E: Stat., Nonlinear, Soft Matter Phys.*, 2009, **79**, 046317.

33 A. R. Bausch and K. Kroy, *Nat. Phys.*, 2006, **2**, 231.

34 F. Jülicher, K. Kruse, J. Prost and J.-F. Joanny, *Phys. Rep.*, 2007, **449**, 3.

35 V. Kantsler and R. E. Goldstein, *Phys. Rev. Lett.*, 2012, **108**, 038103.

36 L. E. Becker and M. J. Shelley, *Phys. Rev. Lett.*, 2001, **87**(19), 198301.

37 E. Wandersman, N. Quennouz, M. Fermigier, A. Lindner and O. du Roure, *Soft Matter*, 2010, **6**(22), 5715–5719.

38 Y.-N. Young and M. J. Shelley, *Phys. Rev. Lett.*, 2007, **99**(5), 058303.

39 P.-G. de Gennes, F. Brochard-Wyart and D. Quere, *Capillary and Wetting Phenomena: Drops, Bubbles, Pearls, Waves*, Springer, 2003.

40 M. Nicolson, in *Proc. Cambridge Philos. Soc*, Cambridge Univ Press, 1949, vol. 45, pp. 288–295.

41 D. Chan, J. Henry and L. White, *J. Colloid Interface Sci.*, 1981, **79**, 410.

42 L. Botto, L. Yao, R. Leheny and K. Stebe, *Soft Matter*, 2012, **8**, 4971.

43 L. Botto, E. P. Lewandowski, M. Cavallaro and K. J. Stebe, *Soft Matter*, 2012, **8**, 9957.

44 E. Furst, *Proc. Natl. Acad. Sci. U. S. A.*, 2011, **108**, 20853.

45 M. Cavallaro Jr, L. Botto, E. Lewandowski, M. Wang and K. Stebe, *Proc. Natl. Acad. Sci. U. S. A.*, 2011, **108**, 20923.

46 E. Lauga and T. Powers, *Rep. Prog. Phys.*, 2009, **72**, 096601.

47 A. E. H. Love, *A Treatise on the Mathematical Theory of Elasticity*, Cambridge University Press, 1892.

48 S. Deboeuf, M. Adda-Bedia and A. Boudaoud, *Europhys. Lett.*, 2009, **85**, 24002.

49 M. Adda-Bedia, A. Boudaoud, L. Bou and S. Debuf, *J. Stat. Mech.: Theory Exp.*, 2010, **2010**, P11027.

50 R. Dreyfus, J. Baudry, M. L. Roper, M. Fermigier, H. A. Stone and J. Bibette, *Nature*, 2005, **437**, 862.

51 A.-K. Tornberg and M. J. Shelley, *J. Comput. Phys.*, 2004, **196**, 8.